2005-01

Physical Limits to Spatial Resolution of Optical Recording: Clarifying the Spatial Structure of Cortical Hypercolumns

Physical limits to spatial resolution of optical recording: Clarifying the spatial structure of cortical hypercolumns

Jonathan Polimeni, Domhnull Granquist-Fraser, Richard Wood, and Eric Schwartz

January, 2005

Technical Report CAS/CNS-2005-007

Boston University Center for Adaptive Systems
and
Department of Cognitive and Neural Systems
677 Beacon Street
Boston, MA 02215

BOSTON UNIVERSITY

COMPUTER VISION AND COMPUTATIONAL NEUROSCIENCE LAB

http://eslab.bu.edu

Physical limits to spatial resolution of optical recording: Clarifying the spatial structure of cortical hypercolumns

Draft 2.6, December 2, 2005

Jonathan R. Polimeni, Domhnull Granquist-Fraser, Richard J. Wood, and Eric L. Schwartz

Abstract Neurons in macaque primary visual cortex are spatially arranged by their global topographic position and in at least three overlapping local modular systems: ocular dominance columns, orientation pinwheels, and cytochrome oxidase (CO) blobs. Individual neurons in the blobs are not tuned to orientation, and populations of neurons in the pinwheel center regions show weak orientation tuning, suggesting a close relation between pinwheel centers and CO blobs. However, this hypothesis has been challenged by a series of optical recording experiments. In this report, we show that the statistical error associated with photon scatter and absorption in brain tissue combined with the blurring introduced by the optics of the imaging system has typically been in the range of 250 μm. These physical limitations cause a *systematic* error in the location of pinwheel centers because of the vectorial nature of these patterns, such that the apparent location of a pinwheel center measured by optical recording is never (on average) in the correct *in vivo* location. The systematic positional offset is about 116 μm, which is large enough to account for the claimed mis-alignment of CO blobs and pinwheel centers. Thus, optical recording, as it has been used to date, has insufficient spatial resolution to accurately locate pinwheel centers. The earlier hypothesis that CO blobs and pinwheel centers are co-terminous remains the only one currently supported by reliable observation.

Keywords hypercolumn model, orientation maps, visual cortex, cytochrome oxidase blobs

---

Introduction

The columnar organization of the neocortex is one of the seminal discoveries in neurobiology [1, 2]. Neurons in vertical register within the cortex tend to have similar response properties, such as selectivity for oriented visual stimuli and ocular dominance [2]. Perhaps even more important, however, was the discovery that columns were themselves organized into larger structures, termed *hypercolumns*, comprised of the full 180° range of orientation tuning for both eyes on the scale of roughly one millimeter [3, 4]. This idea has proven vital since it suggested a basic uniformity of cortical structure and a principle around which it might be organized. Because hypercolumn structure is critical to theories of both cortical function and its development, clarifying its details has been a central goal of neuroscience.

Horton and Hubel [5, 6] showed that an additional periodic anatomical feature of primate visual cortex, the cytochrome oxidase (CO) *blob* system, consists of "patches" of cortical tissue most prominently appearing in Layers II/III, but also appearing in Layers I, IVb, V, and VI, with a size of about 150 by 250 μm in primary visual cortex (V1) of macaque, and exhibiting higher than average metabolic activity, hence, staining darkly for CO activity. They observed the CO blob density to be about five per mm^2, although Horton and Hocking [7] showed variation of a factor of two across subjects. The receptive field properties of neurons in the blobs is still an area of active research, but Livingstone and Hubel demonstrated that unoriented, chromatically tuned receptive fields are a characteristic feature of neurons located within the blobs [8]. Through careful alignment of anatomical data, Horton and Hubel [5, 6] found that CO blobs generally lie at the centers of ocular dominance columns and have an average period, in macaque, of about 350 μm in the direction parallel to local ocular dominance column boundaries and 550 μm perpendicular, demonstrating an inter-relationship between these two anatomical systems that inspired the incorporation of the blob system into a revised hypercolumn model [6, 8].

The "pinwheel" pattern [9] of orientation tuning columns in visual cortex, first observed with optical recording [10, 11], is arguably the single most widely recognized icon of cortical functional architecture. This pattern represents the spatial layout of neurons in visual cortex responsive to oriented visual stimuli, characterized by "orientation singularities" at the pinwheel centers (where locally the map exhibits tuning to the full 180° of orientations) surrounded by regions where orientation preference changes smoothly.

Optical recording studies have shown that pinwheel centers, like the CO blobs, are aligned with ocular dominance column centers in macaque V1 [10, 12]. The neurons within the CO blob regions are not tuned to orientation, and the centers of cortical pinwheels—at least at the level of population response—are also weakly tuned to orientation. The hypothesis that CO blobs and pinwheel centers are co-terminous was thought to establish the basic structure of the cortical hypercolumn. (This hypercolumn model had been suggested previously by Horton [ref. 6, figure 49] and by Blasdel [ref. 13, figure 14].)

However, this parsimonious version of the hypercolumn is inconsistent with three experimental reports. Bartfeld and Grinvald [14] reported evidence, based on joint *in vivo* optical recording of intrinsic signals and CO histology in macaque V1, that CO blobs and orientation pinwheels are not aligned. In apparent support of this observation, they also reported that orientation tuning of neurons near the putative pinwheel centers was no different than those in more distal locations. However, no spatial error analysis was presented in this work.

The latter of these two observations of Bartfeld and Grinvald [14] was followed up, in greater detail, by Maldonado *et al.* [15]. They used a combination of tetrode electrophysiology and optical recording of intrinsic signals in cat areas 17 and 18 to claim that orientation tuning in the pinwheel centers is as strong as in the surrounding area. Maldonado *et al.* [15] supported their claim by pointing out that the optical recording signal is a population average, and so individual neurons in the pinwheel centers—even if they were strongly tuned to orientation—would average to a weak population response at the pinwheel centers imaged through optical recording. However, these authors also did not discuss potential consequences of spatial blur in optical recording, nor did they provide any detailed error analysis of their observations. Although the experiment of Bartfeld and Grinvald [14] was in primate, and that of Maldonado *et al.* [15] was in cat, these two results are widely seen to make the seemingly consistent argument that orientation tuning at pinwheel centers is *strong*. Since CO blobs exhibit little or no orientation tuning, this purported strong orientation tuning at the pinwheel centers is consistent with the hypothesis that pinwheel centers do not coincide with the CO blobs.

In support of the observations of Grinvald and colleagues, a recent joint *in vivo* optical recording of intrinsic signals and CO histology experiment performed in owl monkey V1 by Xu *et al.* [16] estimated that pinwheel density is roughly twice that of CO blob density. If the densities of these two systems were to differ markedly, the systems could not be in one-to-one alignment.

Grinvald and colleagues [14, 17] have rejected the previously established *classical model* that pinwheel centers and CO blobs are aligned. In its place, they suggested an alternate hypercolumn model, based on their optical recording observations, that depicts the pinwheel centers and the CO blobs staggered and out of alignment. This hypothesis has been widely accepted, and now appears in textbooks [see, e.g., ref. 18]. In this report, we show that a careful quantification of the physical limits to the spatial resolution of optical recording based on an analysis of photon scatter and macroscope optics, combined with an understanding of the mathematical properties of orientation maps, demonstrates that there is insufficient spatial resolution in optical recording—as it has generally been used to date—to reject the classical model.

Establishing the precise alignment of sub-millimeter modular systems in the brain requires a careful error analysis, since systematic errors in the range of even 100 μm could lead to false displacement of two different modular systems. One source of error is the unavoidable fact that any optical system has finite spatial resolution, and thus introduces non-zero spatial blur. The point-spread function (PSF), characterized by its full-width at half-maximum (FWHM), is a common measure of the spatial resolution of an optical system. The physical lower limit for the PSF of optical recording is provided by the joint effects of photon scatter in the turbid cortical tissue and the depth-of-field of the optical system.

It is important to clarify the details of spatial resolution and identify sources of spatial filtering because of the vectorial nature of cortical orientation maps. Blur (i.e., spatial averaging) is usually considered in terms of a scalar-valued image source, e.g., a conventional photograph. However, cortical orientation maps that encode both magnitude and orientation at each pixel, are *vector-valued images*. The peaks in a scalar-valued image, such as a photograph, will have negligible positional error associated with isotropic Gaussian blur: the center of a blurred spot will be, on average, in the correct position. However, a vector-valued image, such as a cortical orientation map, has a systematic positional error associated with spatial blur.

The easiest way to understand the difference between blurring scalar- and vector-valued data is to note what happens when one attempts to arithmetically average orientations. (Recall that orientation is defined between 0° and 180°.) The average of the *numbers* 0 and 180 is 90. However, the average of the *orientations* 0° and 180° is not 90° but rather 0° (or 180°). This phenomenon is often called *phase wrapping* in one-dimensional signal processing. Orientations do not obey the same rules of arithmetic as "numbers". As a consequence, blur induces non-zero mean error for singularity location in vector-valued images [Schwartz, E. L. and Rojer, A. S., *Soc. Neurosci. Abstr.* **18**, 742 (1992); see also refs. 19, 20]. (A computer animation illustrating the behavior of orientation maps due to various amounts of spatial blur, which is discussed in detail below, can be seen in Movie 1 and Fig. 4, which are available at http://eslab.bu.edu/publications/polimeni2005physical/.)

To date, the only detailed experimental measurement of the resolution of optical recording (that we are aware of) was provided by Orbach and Cohen [21], who report a PSF of 200 μm FWHM calculated based on imaging a pinhole in aluminum foil through 500 μm of resected salamander olfactory bulb.

Contradicting this experimental result, several authoritative reviews of optical recording report estimates that are much smaller than the measurement of Orbach and Cohen. For example, one review states that the resolution of optical recordings is in the range of 50–100 μm [22]. Another, that it is "better than" 50 μm [17]. These claims were not supported by any accompanying computational or experimental evidence.* Moreover, these same reviews state that one advantage of the narrow depth-of-field of the macroscope is that the vasculature on the cortical surface is removed by defocus: the depth-of-field is so narrow that relatively large blood vessels are blurred enough that they vanish. Since columnar structure in the brain is extensive in depth (so that the entire vertical extent of a cortical column can never be simultaneously in focus), the neuronal response, as well as surface vessels, will also experience significant blur. One of the chief goals of the present work is to analyze this optical blur, as well as unavoidable photon scatter, in detail.

In this report, we show that the statistical error associated with photon scatter and absorption in *in vivo* brain tissue combined with the optics of the imaging system, assuming standard experimental parameters, is in the range of 250 μm FWHM. Associated with the PSF is a systematic error in the location of pinwheel centers and a reduction in their density due to the vectorial nature of these patterns. Because this positional error is systematic rather than merely statistical, the apparent location of a pinwheel center measured by optical recording is never (on average) in the correct *in vivo* location. We estimate the magnitude of the mean systematic positional offset to be about 116 μm for standard experimental parameters. This offset is large enough to account for the claimed mis-alignment of the two columnar systems. Since the application of spatial filters in post-processing is typical in optical recording data analysis [e.g., ref. 16], we also illustrate the effects of band-pass post-process filtering, which are as problematic as the low-pass filtering associated with the physical lower limit for resolution. The error induced by post-processing depends on the signal-to-noise-ratio (SNR) and the parameters of the spatial filters. We show, assuming a wide range of SNRs and commonly employed filters, that post-processing can inflate the pinwheel density by as much as 100% and can introduce substantial positional error in the location of orientation singularities.

* Grinvald and colleagues [14, 17] cite the PSF FWHM measured experimentally by Orbach and Cohen in ref. 21, but claim that the actual resolution of optical recording is two to four times higher than the reported value. They justify the higher resolution by stating that "...if a differential map is calculated, the spatial resolution increases," [ref. 22, p. 4177], and "[the] reproducibility in location of the pinwheel centers suggests, that the resolution of differential optical recording may be better than 50 μm," [ref. 17, p. 34]. No evidence or detailed discussion is presented to corroborate the claim that differential imaging can reduce the point-spread measured by Orbach and Cohen by 400%. It is certainly true that differential imaging improves the signal-to-noise ratio of optical recording since it will reject common-mode noise signals. However, improving the basic PSF of an optical system, i.e., the spatial resolution, requires de-convolution techniques, sometimes called *super-resolution* [23, 24]. Successful de-convolution requires very high signal-to-noise ratio and very good understanding of both the signal and the noise. Neither of these conditions holds for optical recording. Additionally, reproducibility of a measurement is necessary for precision, but is insufficient to guarantee accuracy. An inaccurate measurement, associated with a systematic error, is exactly reproducible. Therefore, the reproducibility over time of optical recording says nothing about the underlying spatial resolution.

Materials and Methods

To determine the physical limits on spatial resolution of optical recording, we used standard Monte Carlo methods [25] to model photon scatter and absorption in gray matter and white matter for photons of wavelength 633 nm (a commonly used optical recording light source) together with a diffractive optics modeling system to study the depth-of-field of the *macroscope* [26] (a lens system commonly used for image acquisition in optical recording) [Granquist-Fraser, D., Polimeni, J., and Schwartz, E. L. *Soc. Neurosci. Abstr.* **29**, 125.3 (2003)]. Our goal was to provide the limiting physical PSF in cortical tissue due to photon scatter and optics. We did not address the additional biological aspects of this problem, which can only make the PSF broader.[†] Therefore, our results provide a conservative physical limit on the best possible spatial resolution obtainable with this technique.

An example of our simulation results for the scattering of 633-nm wavelength photons by a reflectance point source in cortical tissue is illustrated in Fig. 1. Because of the turbid nature of cortex, the trajectories of photons reflected by a point source exhibit a three-dimensional "fuzz-ball" structure depicted in Fig. 1a. Note that photons which ultimately escape cortex—those photons which comprise the image—predominantly exit from shallow tissue depths.

To compute the photon scatter PSF, we calculated, for each location in the three-dimensional model cortex, the probability of a photon scattering to that location from a fixed reflectance point. We also obtained the optical transfer function of the macroscope using an industry standard diffractive optics modeling system (see **Supporting Text** and Figs. 7 and 8). We then combined through convolution the photon scatter distribution with the macroscope transfer function, and averaged over cortical depths from 200 to 500 μm to obtain a "columnar" point-spread function to emulate the response to a signal source emanating from a column of activated neurons. The columnar PSF for a model experiment with a focal depth of 300 μm is presented in Fig. 1b, demonstrating a resulting FWHM of about 240 μm. (Note that the FWHM of the PSF is a function of focal depth—it significantly broadens as the focal point is positioned deeper into cortical tissue [28]. This finding suggests that minimization of optical blur is achieved by focusing near the cortical surface [see, e.g., ref. 29] rather than focusing at 300–600 μm below the cortical surface, as is common.) For reference, in the same plot we show a 50-μm FWHM Gaussian PSF as reported by Grinvald *et al.* [17], and a 280-μm FWHM Gaussian PSF, corresponding to the *in vitro* observations of Orbach and Cohen [21] adjusted to *in vivo* conditions (see **Supporting Text**), and the 240-μm FWHM PSF that was determined from our Monte Carlo simulation of photon scatter and macroscope optics model. The heavy tails of the resultant columnar PSF suggest that the function is better modeled as a Cauchy function than as a Gaussian function—see **Supporting Text** for a discussion comparing these two functions.

The results of our detailed Monte Carlo simulation and diffractive optics model as well as the adjusted experimental measurement of Orbach and Cohen [21] demonstrate that the spatial resolution of optical recording is far lower than the typical estimates. What are the consequences of this lower resolution for the interpretation of the data? We used computational modeling to evaluate the effect of the spatial blur inherent to optical recording on the observed pinwheel pattern.

A simulated pinwheel pattern (see Fig. 9 for details) of periodicity matching the CO blob system (i.e., 350 by 550 μm) was created using band-pass filtered random orientation values [30], and is shown in Fig. 2a. The result of blurring this map with a Cauchy low-pass filter of 240 μm FWHM is shown in Fig. 2b. (Note that blurring the pinwheel pattern is identical to blurring the individual orientation response images that are used to form the pinwheel pattern; see **Supporting Text** and Figs. 10 and 11.) Although the original and blurred pinwheel maps are qualitatively similar in appearance, they are quantitatively very different. (Note also that we have conservatively assumed that there is no spatial noise and no post-process filtering; relaxing these assumptions leads to much greater errors, as shown below.)

Results

Our computer simulation results establish three important effects of spatial filtering on the orientation map spatial structure:

1. Orientation singularities approach, and annihilate, in left- and right-handed pairs when increasing amounts of spatial blur are applied. Therefore, the measured density of pinwheels is significantly reduced and the measured spacing is significantly increased by the blur inherent in optical recording (see **Supporting Text**).
2. Orientation singularity position is systematically offset as a function of spatial blur. The observed pinwheel position is, on average, displaced from the correct *in vivo* position by a mean of 116 μm.

[†] "Microlensing" caused by dense layers of cell bodies has been mentioned as a serious source of optical recording interference [27]. Biological sources of spatial blur include hemodynamics, heart pulsation, and the generally poorly understood nature of the coupling of neural activation to changes in the optical properties of tissue, as well as the underlying noise and spontaneous neural activity.

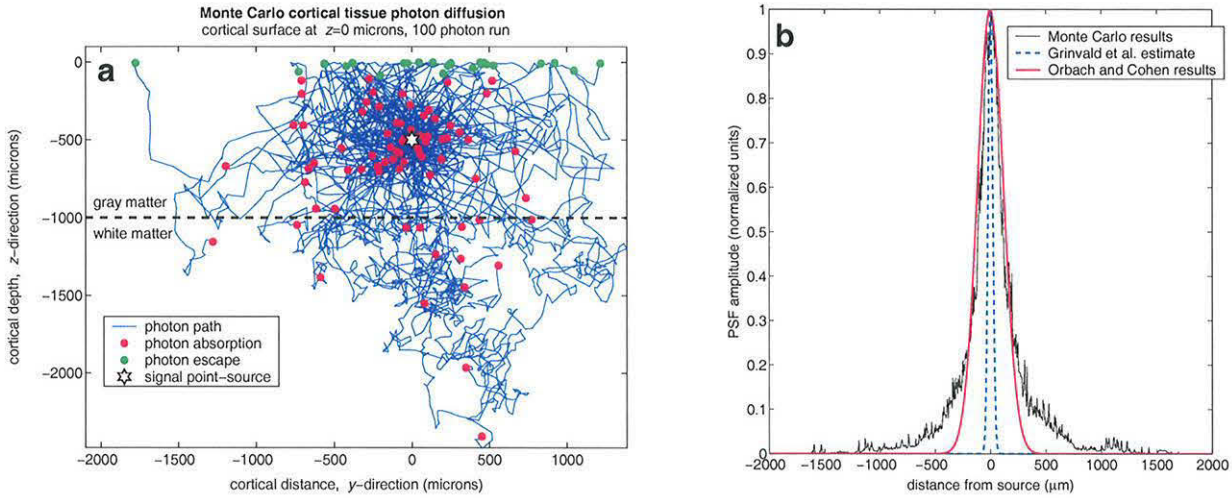

Figure 1: Monte Carlo simulation. (a) Sample of 100 model photon paths in cortical tissue. Cortical gray matter, in this example, was taken to be 1,000 μm thick and the gray matter/white matter interface is denoted by a *dashed black line*. The *white star* marks the model photon source 500 μm below the gray matter/air interface. *Red dots* mark points at which a photon was absorbed. *Green dots* mark points at which photons exit the tissue. The small 1 mm thickness of gray matter illustrated here demonstrates the qualitative difference as the model photon travels through gray matter verses white matter. However, in our simulations, cortical gray matter of 2.3-mm thickness was used, and each PSF computed from 10^6 photons per reflectance source. (b) Resultant columnar PSF, averaged over sources at 200–500 μm cortical depth, with macroscope focus set at a depth of 300 μm. The FWHM is 234.3 μm. Also shown are a 280-μm FWHM Gaussian function, which is the result of Orbach and Cohen [21] (corrected by our Monte Carlo results for missing back-scatter), and a 50-μm FWHM Gaussian function, which is suggested as a possible value by Grinvald *et al.* [17].

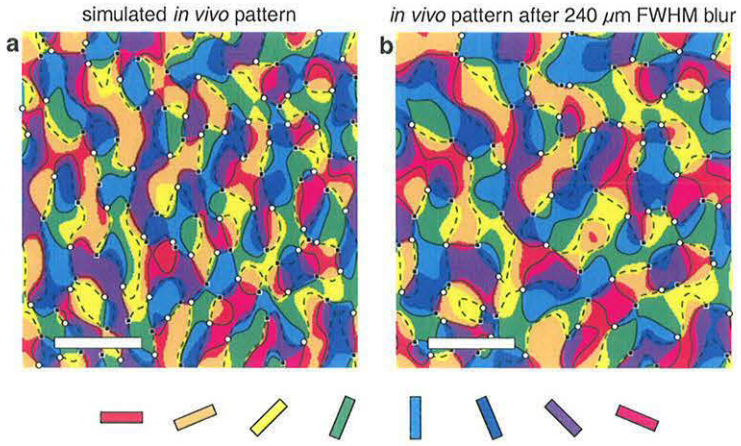

Figure 2: Results of blurring orientation data. (a) Synthetic orientation tuning data generated by band-pass filtering random orientation values [30]. The original average distance between pinwheel centers is set at 350 μm by 550 μm, and the number of pinwheels is 124. Positive chirality (i.e., right-handed) pinwheels are indicated by *white circles* and negative chirality by *black squares*. The *solid* and *dashed black lines* trace out zero-crossings of the orientation map, whose intersections mark the pinwheel center locations for a continuous orientation map—a result known as the sign theorem [31]. (b) Blurring the data of (a) with a Cauchy filter whose FWHM is 240 μm results in an average pinwheel distance of 499.1 μm and 93 pinwheels. If the pattern in (a) is taken as the true *in vivo* orientation map, the pattern in (b) is that one that would be produced by imaging with the blur that we have estimated from our joint photon scatter simulations and optics model. The pseudo-color map of orientation is provided below. In both panels, the scale bar represents 1 mm.

3. Orientation response far from singularities are more spatially stable under blur than that near pinwheel centers.

The systematic error associated with low-pass filtering orientation maps was studied by varying the presumed blur over a large range, and generating 1,000 simulated orientation maps for each FWHM. The results are summarized in Fig. 3a. For a simulated *in vivo* pinwheel pattern with 350 by 550 μm periodicity and a Cauchy-distributed spatial blur with FWHM of 240 μm, both the density and the total number of pinwheels is reduced through annihilation of neighboring right- and left-handed pinwheels by about 25%, and a systematic bias in their position of 116 μm is introduced. The results for the full range of blurs is shown in Fig. 3a, and is illustrated in Movie 1.

Our results indicate (*i*) pinwheel density, in the absence of spatial noise and post-processing, is underestimated by an amount determined by the magnitude of blur in the imaging technique and the veridical *in vivo* spacing; and (*ii*) the observed position of pinwheel centers is systematically offset from the true position by the imaging blur. This is a bias—a non-zero mean error—in the blurred data. This finding means that the optically imaged position of a cortical pinwheel is never correct, but that it is offset from the true *in vivo* location.

These results require a re-interpretation of the observations of Bartfeld and Grinvald [14] and of Maldonado *et al.* [15]. In the case of the Bartfeld and Grinvald [14] experiment, the pinwheel patterns generated by their optical recording are blurred versions of the true cortical pinwheel patterns and are therefore subject to the same pinwheel center offset that we see in simulation. Therefore, one can expect an average displacement of the observed pinwheel centers from their true locations on the order of 116 μm, which is enough to shift the pinwheel centers outside of the blob regions if the pinwheel centers and the CO blobs were truly aligned as in the classical model. Based on this argument, the results of the Bartfeld and Grinvald [14] experiment are insufficient to disprove that the two systems are aligned.

A further illustration of the scale of CO blobs in the macaque *vis-à-vis* the systematic error in pinwheel location is shown in Fig. 3b. Here, a synthetic pinwheel pattern, computed based on typical macaque parameters, is displayed with a 100-μm radius circular ring representing a CO blob centered on a pinwheel center. The "spotlight" superimposed on the pinwheel pattern above the CO blob region represents the reported 65-μm radius recording area of the tetrode (as used in the cat by Maldonado *et al.*[15]) displaced 116 μm away from the pinwheel center. This illustration demonstrates that the 116-μm pinwheel center displacement predicted by our simulations is sufficient to shift their tetrode placement enough for the tetrode recording area and the actual CO blob region to exhibit little overlap.

Pinwheel center offsets of this magnitude may also account for the observed range of orientations near pinwheel centers reported by Maldonado *et al.* [15] in the cat. The expected result for a tetrode placed at a pinwheel center would be to observe nearly a full 180° range of tuning in the neighborhood of the tetrode. We find that a 240-μm blur yields an average pinwheel offset of about 116 μm, and this would correspond, within a tetrode recording radius, to an average observed orientation range of 43.2° (based on macaque pinwheel spacing parameters), which is very similar to the range reported by Maldonado *et al.* [15] of 39.2° at the (purported) pinwheel centers. Had their tetrode been placed at an actual pinwheel center, an orientation range of 180° would be expected. This analysis supports our hypothesis that their tetrode was systematically located in a region of the cortex significantly distant—perhaps up to 100 μm—from the actual *in vivo* pinwheel center. (The results of our tetrode experiment simulation are presented in Fig. 5.) It is likely that the optical recording data systematically misguided their tetrode placement such that observations of cells exhibiting strong orientation tuning were made from cells that were not in fact located in the true pinwheel centers.

The results presented thus far have only assumed sources of spatial blur attributable to purely *physical* phenomena, namely photon scatter in tissue and optical point-spread. These results, therefore, ultimately speak to the physical limitations of optical recording and the effects of its resolution on the analysis of orientation maps. It is common practice, however, to intentionally introduce spatial filtering during data post-processing to eliminate unwanted spatial noise. This filtering can affect the position and density of orientation singularities and thus can impact observations on the alignment of the pinwheel pattern and CO blob system.

In Fig. 6, we briefly present the consequences of applying band-pass post-process filters employed in the recent Xu *et al.* [16] study that reported a higher density of orientation singularities than CO blobs. Our simulation shows that even assuming unrealistically high signal-to-noise ratios (in the range of 10–100), applying the same band-pass post-process filters employed by Xu *et al.* [16] introduces artifactual pinwheels—nearly doubling the initial density—and induces substantial positional error for the orientation singularities. As demonstrated by the results shown in Fig. 6, this effect is strongly dependent on the spatial SNR of the data, with smaller SNR increasing the error. Thus, even though Xu *et al.* [16] took steps, following the recommendations in a preliminary version of this report [Granquist-Fraser, D., Polimeni, J., and Schwartz, E. L. *Soc. Neurosci. Abstr.* **29**, 125.3 (2003)], to minimize physical blur by focusing shallowly in the cortical tissue during optical recording, their use of post-process filters undermines their conclusion that the pinwheel and CO blob systems are mis-aligned.

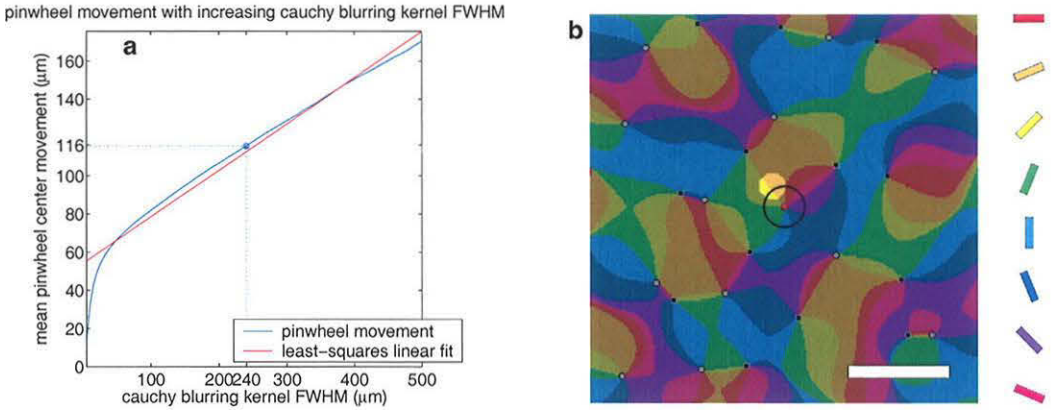

Figure 3: Effects of blur on pinwheel center position. (a) Simulation of pinwheel movement and annihilation due to low-pass filtering with increasing FWHM to 1,000 *in vivo* pinwheel patterns with 350 × 550 μm spacing. As the Cauchy blurring kernel broadens, the average pinwheel movement increases nearly linearly, resulting in a bias in the observed singularity location relative to the true *in vivo* location of the singularity. At 240 μm FWHM, the orientation singularity position error is 116 μm on average. (b) Simulation of the experiment of Maldonado *et al.* [15]. The offset of the tetrode recording site from the true orientation singularity location is demonstrated on a synthetic orientation tuning preference map. Here, the tetrode is illustrated by a *spotlight* of radius 65 μm offset from a orientation singularity by 116 μm. In this example, the tetrode observes an orientation range of about 40°. The *black ring* marks the area of a CO blob with 100 μm radius centered at the chosen orientation singularity, and the areas of the tetrode recording and the CO blob exhibit little overlap. The scale bar represents 500 μm.

Discussion

Optical recording, when used to image scalar-valued distributions such as the intensity patterns measured in visual topography experiments [32], is much less sensitive to resolution limits than vector-valued images since scalar-valued images are expected to have an approximately zero-mean error associated with blur. Additionally, a significant component of the spatial blur analyzed here is caused by the macroscope due to its very narrow depth-of-field [26]. Although the large light-gathering properties of this instrument are an advantage for many applications, it is perhaps not the best choice of optics for sensitive spatial measurement of vector-valued patterns. Furthermore, the common practice of focusing at depths significantly below the very top layer of cortex, where photons escape into the instrument, is a significant cause of error.

Scalar-valued imaging was used in several optical recording experiments [33, 34] to locate CO blobs *in vivo*. This approach is expected to be free of the systematic location error associated with using the pinwheel formalism. By using the blob imagery as a guide, it should be possible to make extensive electrode penetrations in a small number of blob regions and the corresponding extra-blob regions. If additional errors related to parallax and to alignment of *in vivo* and *in vitro* anatomical patterns were carefully handled, the details of blob and extra-blob hypercolumn structure could be further clarified by this approach.

Voltage-sensitive dye imaging [35] has the same physical limits on resolution from photon scatter and optics as intrinsic optical recording. However, limiting the vertical range of dye penetration to superficial cortex could provide the benefit of limiting the extension in depth of the optical source. Then, appropriate focus of the optical system would provide a considerably more favorable "columnar" PSF. An emerging high-resolution imaging technique that uses laser-scanning fluorescence microscopy with multiphoton excitation avoids the problems of photon scatter since all photons collected from a particular scan position emanate from a single excitation point in the tissue [ref. 27; see also Ohki, K., Kara, P., and Reid, R. C., *Soc. Neurosci. Abstr.* **30**, 646.2 (2004)].

Optical recording is a major addition to the tools available for exploring functional neuroanatomy. However, until recently, there has been little appreciation of the dependence of results obtained with optical recording—particularly the imaging of vector-valued orientation maps in visual cortex—on spatial resolution. The effective spatial filter that has been derived in this report, from Monte Carlo simulation and diffractive optics modeling, depends in a complicated way on the wavelength of light, the depth-of-field of the optics, the choice of focal depth, and the extent of vertical summation. By illuminating with light at 633-nm wavelength, imaging through macroscope optics, and assuming a columnar structure that extends from 200 to 500 μm, we have found that the effective FWHM of the physical component of blur is about 250 μm at a focal depth of 300 μm. This finding argues that optical recording resolution is much coarser than is commonly assumed, which leads to serious errors in the estimation of the quantitative properties of orientation maps. Post-process spatial filtering, which is widely used, can cause large additional variations in observed pinwheel center

density and position.

Our results are comparable to those provided by Orbach and Cohen [21], as well as with the recent Monte Carlo study of Deng and Gu [36], who found a PSF FWHM of about 350 μm for 400-nm wavelength light at a focal depth of 500 μm with a 0.25 numerical aperture lens. We emphasize that the experiment of Orbach and Cohen and the simulation of Deng and Gu refer to slightly different conditions than those that we studied, which are specific to the macroscope and to columnar neuronal structure. Nevertheless, all three results suggest a spatial resolution in the range of 300 μm FWHM.

Error analysis in this area has been neglected, and must become a standard requirement for quantitative study of hypercolumn structure. In this context, it would be extremely desirable to directly measure the columnar PSF, for example, by imaging fluorescent beads embedded in tissue at different cortical depths. Then, the analysis and simulation methods outlined here could be used as a guide to establish error bounds for individual experiments for the specific optics, wavelength, and depth-of-focus used.

The conclusion of our analysis is that optical recording, as it has been used to date, does not have sufficient accuracy to determine the spatial relationship between the CO blob and the orientation pinwheel systems. Hopefully, techniques, such as multi-photon optical recording, will succeed in resolving this issue which is central to understanding the functional architecture of visual cortex. At the present time, at least one detailed microelectrode study [8] has affirmed what we term the *classical model* for the cortical hypercolumn: *cells in CO blobs exhibiting poor orientation tuning lie at the centers of orientation pinwheels, and CO blobs and pinwheel centers spatially coincide.* Subsequent rejections of it, through optical recording methods, are clouded by methodological problems, and do not stand up to the conservative error analysis provided in this paper.

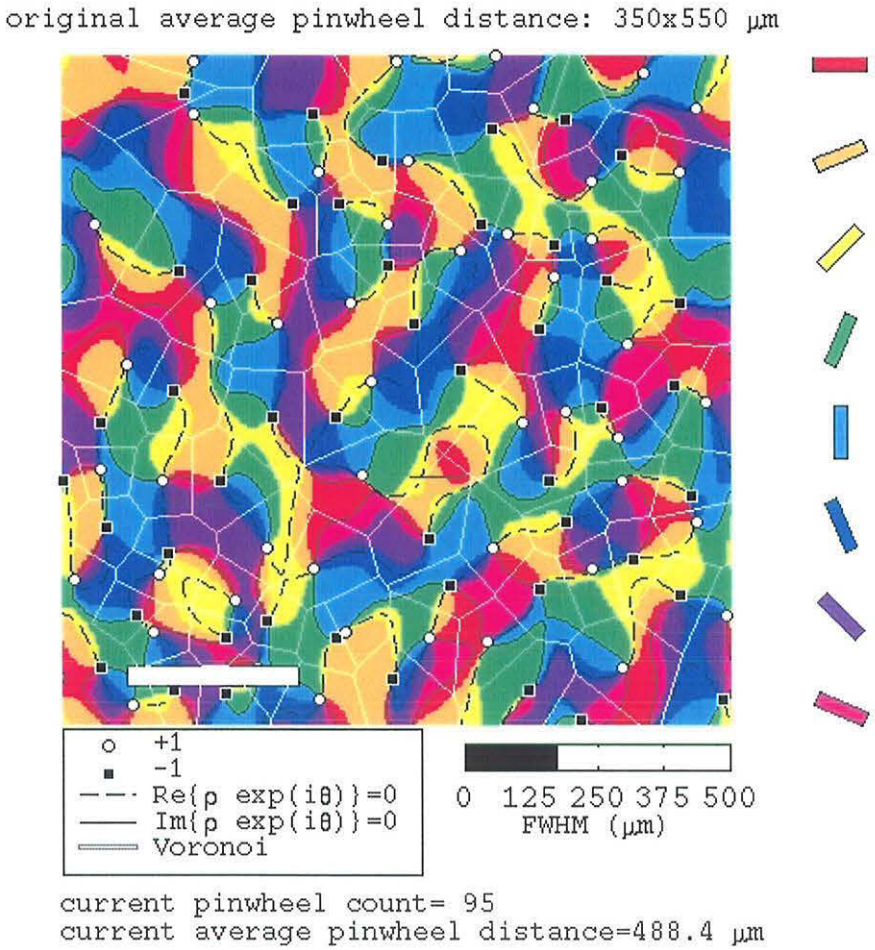

Figure 4: Animation of orientation tuning map under blurring. Example frame of animation depicting the orientation map shown in Fig. 2 of the accompanying report under blurring of successively broader low-pass filters. The filter applied to the *in vivo* map was an isotropic Cauchy kernel parameterized by its FWHM. The blurring filter is increased in 20 25-μm steps from 0 μm (which corresponds to the initial or *in vivo* pattern) to 500 μm, resulting in twenty-one frames of animation. Positive chirality (i.e., right-handed) pinwheels are indicated by *white circles* and negative chirality by *black squares*, both placed at the pinwheel centers. The *solid and dashed black lines* trace out zero-crossing contours of the real and imaginary components of the complex orientation map, respectively. Note that the orientation singularities occur at intersections of the two families of zero-crossings, as described in the accompanying report. It has been shown that left- and right-handed orientation singularities are nearest neighbors (both in simulation and using actual optical recording data; see ref. 31) along the zero-crossing lines of the complex orientation map. In addition, the Voronoï diagram [37] of the pinwheel centers has been provided as *white lines* to aid in the visualization of the pinwheel migration and annihilation. Each frame is 256×256 pixels, and each pixel represents about 15 μm, therefore each frame represents just under 3.9×3.9 mm. The scale bar in the lower left corner of each frame represents 1 mm of cortex, and the pseudo-color map of orientation labels is displayed on the right. (This computer animation is available as Movie 1 at our laboratory web site, http://eslab.bu.edu/publications/polimeni2005physical/, in several animation file formats.)

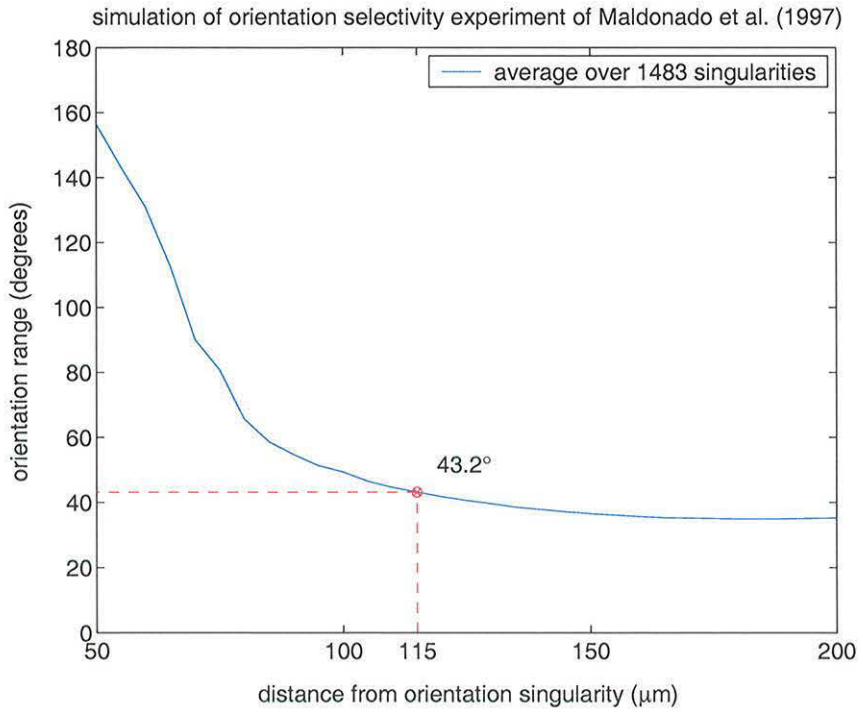

Figure 5: Orientation range as a function of pinwheel offset. In the accompanying report, we present the results of our simulation of an experiment carried out by Maldonado *et al.* [15], who used a combination of tetrode electrophysiology and optical recording of intrinsic signals in cat areas 17 and 18 to measure the orientation tuning strength in the pinwheel centers. Our simulation of this experiment consisted of generating several synthetic pinwheel patterns, then for each pinwheel pattern measuring the orientation range that would be seen by a tetrode recording from the pattern as a function of distance from pinwheel centers. Here we show the recorded orientation range measured from a tetrode (whose recording radius is assumed to be 65 μm, as is claimed by Maldonado *et al.* [15]) as a function of the distance from the tetrode recording site to the nearest true *in vivo* pinwheel center. For a Cauchy kernel of 240 μm FWHM, the mean singularity shift is approximately 116 μm. Our simulations show that, under a 116-μm offset, the mean orientation range is 43.2°, whereas Maldonado *et al.* [15] report an orientation range of 39.2° at the (purported) pinwheel centers. Based on this figure, at a distance of 50 μm from the veridical pinwheel center (a widely cited estimate for the accuracy of optical recording) an orientation range of 160° would be observed via tetrode recording, and at distances as far as 200 μm the orientation range would still be similar to that reported by Maldonado *et al.* [15]. The curve shown has been generated from nearly 1,500 pinwheel centers taken from synthetic data generated with an average pinwheel center spacing of 450 μm.

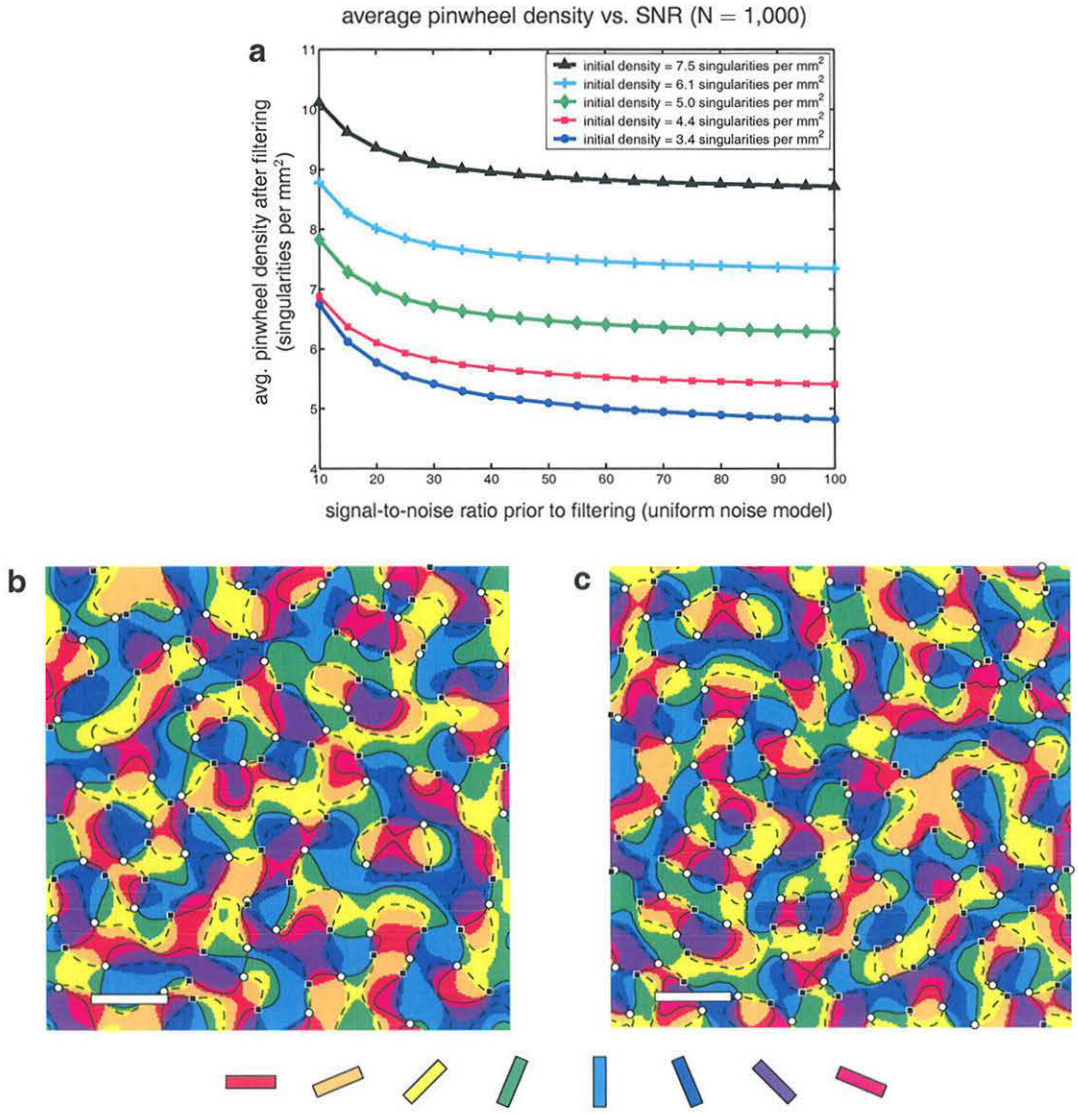

Figure 6: Effects of post-processing on orientation singularity density and position. (a) Results of a simulation investigating the effects of post-process filtering on observed average pinwheel density as a function of signal-to-noise ratio (SNR). This simulation was modeled after a recent optical recording experiment on owl monkey visual cortex performed by Xu *et al.* [16] in which the investigators convolved their raw data images with a 40 μm radius mean filter kernel and with a 450 μm radius mean filter kernel, then subtracted the results. This band-pass filtering was applied to reduce unwanted spatial noise. Xu *et al.* [16] also report that the average CO blob spacing observed in V1 of their subjects was 3.6 blobs per mm^2. Our simulation consisted of first generating 1,000 synthetic pinwheel maps whose pinwheel densities were set at 3.6 singularites per mm^2, then adding uniform spatial noise to the patterns at increasing noise levels (determined by the noise variance), and finally filtering the noisy patterns with the post-processing band-pass filter specified by Xu *et al.* [16] and then calculating the resulting average pinwheel density across all trials. For comparison, we have also included results of simulations using several different initial pinwheel densities. Our simulation results demonstrate that the spatial noise patterns present in the raw images introduce artifactual pinwheels after band-pass filtering, and therefore typical post-processing techniques, such as those employed by Xu *et al.* [16], can lead to over-estimates of pinwheel density when the pinwheel counts are taken from band-pass filtered data. (b) A synthetic orientation map with 3.47 singularites per mm^2. (c) The pinwheel map shown in (b) after adding a small amount of uniform spatial noise to yield an SNR of 100 and band-pass filtering with the post-processing filter used by Xu *et al.* [16]. The resulting pinwheel map has a singularity density of 4.66 singularities per mm^2. Note that the original map in (b) and the post-processed noisy map in (c) qualitatively look strikingly different. This demonstrates that, even in cases with high SNR, *post-process filtering can greatly affect both the density and position of orientation singularities due to the sensitivity of these complex-valued patterns to spatial blurring*, as discussed in the accompanying report. Thus, even if the pinwheel and CO blob systems spatially coincide in the owl monkey striate cortex, as studied by Xu *et al.* [16], this post-process filtering could introduce sufficient distortion of the final pinwheel pattern to throw these two systems out of alignment and artificially inflate the observed pinwheel density. The pseudo-color map of orientation is provided below. In panels (b) and (c), the scale bar represents 1 mm.

Supporting Text

Our investigation into the spatial blur in optical recording consisted of a joint Monte Carlo simulation of photon scatter and absorption in cortical tissue and a diffractive optics model of the macroscope. The full details of our system have been presented elsewhere [28]. Here we review the most relevant details of the system, and describe our quantitative analysis of cortical orientation maps.

Monte Carlo Methods

Monte Carlo techniques are the primary method for modeling the behavior of light in biological tissue. They were first applied in this context to modeling the interaction of laser light with tissue in medical applications for the assessment of damage during clinical laser ablation [38]. The term *Monte Carlo* [39] refers to the use of a stochastic simulation to model physical processes. It is well understood and widely deployed. However, since the tissue ablation literature assumes the existence of a tightly collimated laser beam, and the current application requires examination of individual photon paths, we wrote a custom version of the basic photon scattering and absorption model in the MATLAB development environment (MathWorks, Natick, MA).

Tissue optical Parameters

There are four fundamental optical parameters required to accurately model photon propagation in a turbid medium such as visual cortex. These are the coefficient of absorption, μ_a, the coefficient of scatter, μ_s, the index of refraction, n, and the anisotropy constant, g. These parameters, except for the index of refraction, are significantly different in different types of tissue, and the model must account for this by using parameter values measured empirically for gray and white matter in the cerebral cortex. In this simulation, the optical parameters used in the Monte Carlo simulation [see, e.g., ref. 40] were: 1.4 for n in both gray and white matter; 2.7 and 2.2 cm^{-1} for μ_a; 354 and 532 cm^{-1} for μ_s; 0.94 and 0.82 for g, for gray matter and white matter, respectively. All parameters were for light at 633 nm wavelength. In the tissue optics literature, a range of different parameter values have been reported, usually based on measurements taken with excised tissue up to 48 hours post mortem [see, e.g., refs. 41, 42]. The parameter values used in this study were based on measurements taken from freshly resected cortical gray and white matter and therefore provide better estimates for *in vivo* tissue optical parameters.

It has been suggested to us [D. Boas, *personal communication*] that the tissue absorption coefficient μ_a has smaller values *in vivo* than even the freshly resected tissue values indicate, based on observations of an "immediate darkening" of excised cortical tissue when exposed to air. We investigated the consequences of this by performing Monte Carlo simulation runs with values of μ_a 10 times smaller than the published value. The result was an increase in the FWHM of photon scattering due to the participation of photons from deeper positions of origin that were absorbed in the tissue under conditions of larger μ_a. Therefore, the published value of μ_a for freshly resected tissue that we use here provides a conservative lower bound on the width of photon scattering.

Note the qualitative difference in the photon path as the model photon travels through gray matter verses white matter, shown in Fig. 1a of the accompanying report, that results from the model parameter differences between the two tissue types, and the dominance of exit points in the very shallow depths of the tissue—an effect of the absorption probability that tends to prevent deeper photons from emerging without further scatter into the upper layers.

Anatomical Parameters of the Model

The thickness of our model cortex was set at 2.3 mm. Monkey and cat cortex are similar in thickness; the exact value of cortical thickness proved to make little difference in the resulting PSFs due to the strong extinction with cortical depth. The first 500 μm of tissue provide the signal, and the first 200–300 μm is the majority of this contribution. The cortical depth of the model photon source was varied between depths ranging from 100 to 1,000 μm at 50-μm intervals. This range covered those values of focal depth typically used by experimental researchers engaged in the optical recording of intrinsic signals [17] that vary between 300 and 500 μm, but sometimes are deeper (e.g., Womelsdorf *et al.* [43] used a 700-μm focal depth) or shallower (e.g., Schiessl and McLoughlin [29] focus on the cortical surface).

Anisotropic Scattering of the Model Photon

Photon scatter in a turbid medium is biased towards the forward direction—that is, it is not isotropic. The typical model for the anisotropic component of photon scatter in tissue is based on an empirically deduced model, first used to model scatter of light in the interstellar medium, known as the *Henyey-Greenstein phase function* [44]. It is termed a phase function since, in the case of a linear projection, it models the measured time lag for photons to reach the detector. The Henyey-Greenstein phase function is parameterized by the anisotropy coefficient, g, which must be chosen to fit the scattering data. The anisotropy coefficient can vary from a value of $+1$ for complete forward scattering, to 0 for isotropic scatter, to -1 for complete backward scattering.

The Henyey-Greenstein phase function p_{HG} is given by

$$p_{\mathrm{HG}}(\cos\theta) = \frac{1}{4\pi}\frac{1-g^2}{(1+g^2-2g(\cos\theta))^{\frac{3}{2}}}$$

as a function of $\cos\theta$, where θ is the latitude of the photon travel direction. The Monte Carlo sampling function of $\cos\theta$ for the phase function,

$$\cos\theta = \frac{1}{2g}\left[1+g^2-\left(\frac{1-g^2}{1-g+2g\xi}\right)^2\right],$$

was derived by Witt [45].

Optical PSF of the Macroscope

Most single-lens reflex camera lenses of high quality are of a *double gauss* design [see ref. 46]. The layout of the model macroscope [17, 26] used to compute the diffraction PSF contributions to the overall imaging error is a symmetric, $1:1$ relay system consisting of two identical seven-element double gauss single-lens reflex camera lens systems arranged front to front, as shown in Fig. 7. Both lenses are of 50-mm focal length and are in close mechanical proximity in order to minimize diffractive error in the image plane. The particular variant of the seven element double gauss design used in this model was chosen for its specification and performance similarities to the 50-mm Pentax SMCP-FA f/1.4 lens because this lens type and manufacturer are often cited as being used by experimenters collecting optical recording data from cortical tissue [e.g., ref. 17]. The exact lens design used for our model was a design by Y. Fujioka [46, 47].

All wave optics calculations were performed using the Advanced Systems Analysis Program, or ASAP (Breault Research, Tucson, AZ), using the optical design parameters of the Pentax 50-mm lens.

To confirm the results of our Monte Carlo simulation and diffractive optics model discussed above, we constructed a physical macroscope system on an optical bench and imaged a calibration slide through an *intralipid* phantom, which is known to have a scattering cross section very similar to that of freshly resected cortex [48]. The observed blur of the calibration image agreed well with our simulation results, and with existing experimental measurements in cortical tissue.

PSFs of the Macroscope at Varied Tissue Depths

The Gaussian Beam Decomposition method [49] was used to calculate the two-dimensional diffraction PSF at several focal depths including the object plane and several planes above and below the object plane. It was necessary to calculate the out-of-focus planes as the contributions to the total PSF come from the entire volume of the tissue under observation.

For the macroscope optical model, we computed the PSFs for on-axis model photon origin positions at 50-μm intervals. Fig. 8 provides a subset of diffraction PSFs generated for planes above and below the object plane at 150-μm intervals. Each individual PSF image is 600 $\mu\mathrm{m}^2$.

Combined PSF for Photon Scatter and Macroscope Optics

The intensity distribution of photons reflected from a particular point source and reaching the detector through the optical system was produced by convolving the diffraction PSF of the macroscope optics with the three-dimensional distribution of photons associated with a point reflectance source produced by the Monte Carlo photon propagation simulation. This PSF was computed for point source locations and macroscope focal depths that were independently varied between cortical depths of 100–500 μm.

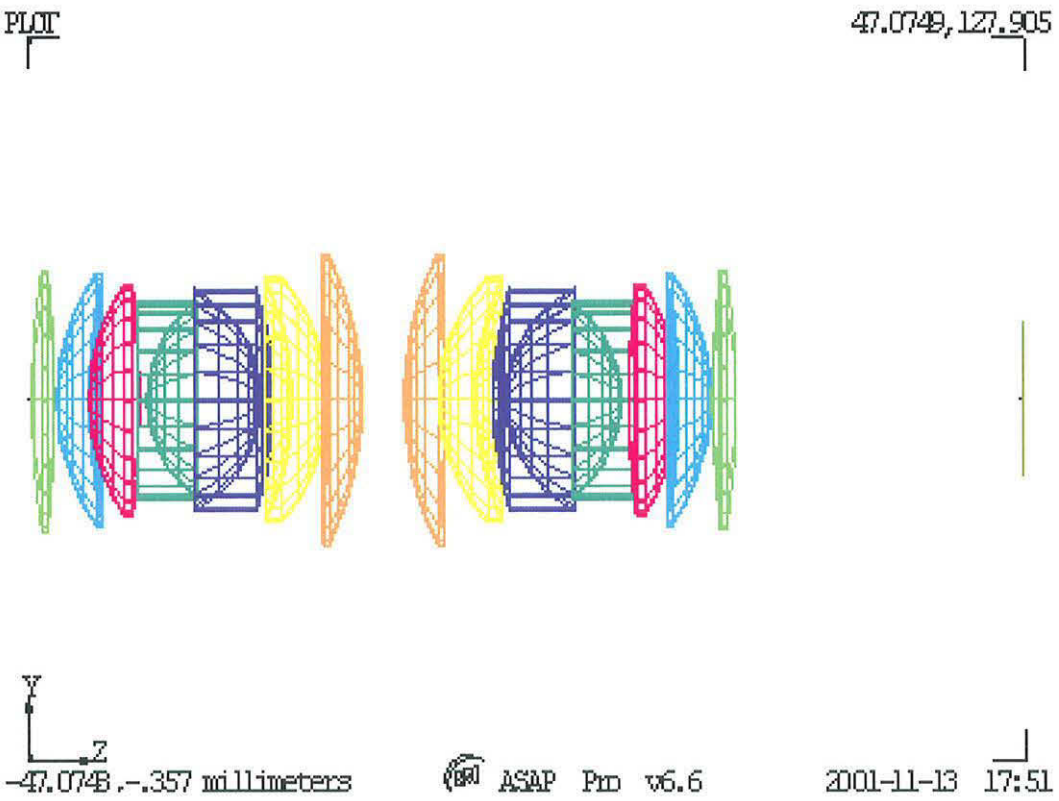

Figure 7: Macroscope lens diffractive optics model. The design of the macroscope is that of two single-lens reflex camera lenses faced front to front giving a wide field-of-view and collecting considerably more light than the standard microscope objective. The optical elements are based on the Pentax 50-mm lens. The line on the far right represents the plane of the detector element.

Figure 8: Macroscope diffraction PSFs. A subset of the macroscope diffraction PSFs computed with ASAP that were used to model the macroscope optics. The numbers beneath each panel denote the distance, in the direction of the optical axis, between the PSF and the focal plane of the macroscope, where 0 μm signifies the PSF at the focal plane, positive values signify PSFs at heights nearer than the focal plane, and negative values signify PSFs at depths farther than the focal plane. The center of each image represents the PSF at the optical axis, and the pixel intensity is proportional to flux per mm^2 of the PSF.

Columnar PSF

The neuronal response to orientation stimuli was taken to be columnar, i.e., identical in response through the supra-granular depths of the cortex, excluding Layer I. Out-of-focal-plane contributions to the optical image signal were modeled by convolving the combined PSF (joint effect of photon scatter and macroscope optics) for point sources averaged over a vertical region between 200 and 500 μm in depth. We omitted summing from Layer I due to the lack of cell bodies and the presumed broadened optical signal from crossing fibers expected in Layer I of cortex. We did not sum from below 500 μm, since our Monte Carlo simulations indicated that the signal attenuation with depth was about a factor of eight for every 100 μm, and thus the signal contributions from lower cortical depths were negligible.

In optical recording experiments, not all cortical depths receive equal illumination since photon scattering and absorption prevent photons entering the cortex from an external light source from penetrating deep into the tissue. As a result, shallow tissue receives much more light than deep tissue, thus the signal originating from deeper cells will have a reduced intensity relative to that from the shallow cells. To estimate the effects of reduced illumination with depth, we simulated photons entering the cortical surface after being emitted from a collimated light source, and calculated the proportion of photons reaching each cortical depth after diffusing through the tissue. We used these photon counts to weight the contributions of individual PSFs from each cortical depth. This provided a more accurate columnar signal that accounts for the effects of realistic illumination.

We term this vertically averaged PSF the "columnar" PSF. Since the columnar PSF represents the joint effect of photon scatter, macroscope optics, illumination, and biological extension of source, the width of this columnar PSF is the final measure of spatial resolution in the current context.

The columnar PSFs computed with our simulations were better approximated by the Cauchy function rather than the Gaussian function, as is expected on *a priori* grounds: beam scattering is often described by the Cauchy (or "Lorentzian") function, i.e., the probability distribution of the horizontal distances at which a line segment chosen with uniform random angle cuts the horizontal axis [50]. Due to the heavy tails found on Cauchy kernels, the Cauchy provides more blur than a Gaussian kernel with the same FWHM. The Gaussian kernel with equivalent blurring capacity to the 240 μm columnar PSF has a FWHM of roughly 300 μm, based on visual evaluation of pinwheel blurring with both Cauchy and Gaussian functions.

Correction for Backscatter

Orbach and Cohen [21] imaged a pinhole in aluminum foil through 500 μm of resected salamander olfactory bulb. The aluminum foil cut off back-scattered photons, which can make a significant contribution to the PSF of a point source in turbid cortical material. We used our Monte Carlo simulation to correct for this back-scatter, which amounted to a 40% increase in the width of the observed PSF at this depth. Therefore, we consider their PSF to be better represented, with respect to *in vivo* measurement for which there is no aluminum foil, by a value of about 280 μm FWHM. Note, however, that this value only represents the PSF, rather than the columnar PSF that we have computed in this work, and that their measurement was obtained using microscope optics rather than macroscope optics.

Analysis of Orientation Maps

Blurring Induces Orientation Singularity Movement

The complex orientation map, as introduced by Blasdel and Salama [10], is a complex-valued function of the form

$$\Omega(x,y) \equiv R(x,y) + iI(x,y) = \rho(x,y)\, e^{i\phi(x,y)},$$

where x and y represent coordinates on the cortical surface. The orientation field $\phi(x,y)$ itself is the "pinwheel pattern" seen in visualizations of the orientation tuning map, however some authors incorporate the $\rho(x,y)$ term into "angle-magnitude maps" [14].

Since the magnitude of the complex orientation map, $\rho(x,y)$, is zero-valued at the orientation singularities (otherwise the complex orientation map would diverge at the orientation singularities where the gradient of $\phi(x,y)$ approaches infinity), those singularities are located at the points where both the real and imaginary parts of the complex orientation map are zero, i.e., at the intersections of the zero-crossings of $R(x,y)$ and $I(x,y)$. The zero-crossing contours of $R(x,y)$ bound regions of $R(x,y)$ that are either all positive or all negative, and likewise for the zero-crossing contours of $I(x,y)$. Averaging the complex orientation map smooths the profiles of the scalar-valued components $R(x,y)$ and $I(x,y)$, causing these positive and negative regions to broaden and change shape, and hence causes zero-crossing contours within both $R(x,y)$ and $I(x,y)$ to shift and migrate.

As the zero-crossing contours migrate, the intersections of $R(x, y)$ and $I(x, y)$ wander, and the pinwheel centers are displaced. Often, neighboring pairs of positive or negative patches coalesce into new, larger regions of positivity or negativity, which is observed as pinwheel *annihilation*. (Rarely, these zero-crossings will wander into new intersection points, resulting in "vortex pair creation", i.e., the spontaneous appearance of a new left-handed–right-handed pinwheel pair.) Detailed discussion of pinwheel annihilation and motion under blur is found in refs. 19, 20, 31. Related mathematical details are discussed in the optics and solid-state physics literature, where analogous phenomena have been thoroughly analyzed during the past several decades [for review see, e.g., refs. 51, 52].

The reason that points within regions far from the singularities are spatially stable is that they typically occur in domains where the magnitude of the complex orientation map is large and slowly changing, e.g., at local maxima of the magnitude of the orientation map. Blurring, or averaging, these regions behaves like the scalar image case, i.e., the "peaks" do not shift very much. However, the intersections of the zero-crossing contours drift considerably. For this reason, it is to be emphasized that any *validation* of optical recording by electrophysiological techniques is sensitive to where in the imaged pinwheel map one places the microelectrode. That is, when guided by the optical recording map microelectrode measurements taken from regions surrounding the pinwheels (i.e., regions of strong orientation response) would be in good agreement with the local optical recording estimates due to the stability of the pinwheel map with respect to blur. However, microelectrode measurements taken from the locations of the pinwheel centers (i.e., regions of weak orientation response) would disagree with the optical recording data due to the lability of the pinwheel centers when exposed to spatial blur. This is the essence of the problem with locating pinwheel centers and evaluating the accuracy of orientation maps, and is illustrated in the computer animation Movie 1 available at `http://eslab.bu.edu/publications/polimeni2005physical/`.

Orientation Singularity Detection

The centers of pinwheels, i.e., the orientation singularities, were detected by locating non-zero points in $\nabla \times \nabla\phi(x, y)$, which can be easily calculated from the orientation map $\phi(x, y)$. It has been frequently stated in the modeling literature [e.g., ref. 53] that the gradient of the orientation map must have zero curl since the differential operator $\nabla \times \nabla$, the curl of the gradient, is identically zero. The gradient of a continuous function must, indeed, have zero curl, but $\phi(x, y)$ is not a continuous function: it is *singular* at the pinwheel centers. In fact, the non-zero points in $\nabla \times \nabla\phi(x, y)$ locate these centers correctly and efficiently. This method of pinwheel center detection was verified by checking that the line integral of $\nabla\phi(x, y)$ is an integral multiple of π at putative singularity locations, i.e., that the magnitude of the winding number of $\nabla\phi(x, y)$ is one [31]. It is mathematically possible that the magnitude of the winding number around an orientation singularity could be greater than one, but we have never observed these, nor have they been observed in the *in vivo* optical recording data [12], presumably because it is statistically unlikely for *multiple* pairs of zero-crossing contours to intersect at a single point.

Distance Between Singularities

Distance between singularities was measured by using the locations of singular points, detected as described above, and constructing the Voronoï diagram and the associated Delaunay triangulation of this point set [37]. Lengths of Delaunay edges were taken to represent the distance of neighboring pinwheel centers. This provides a "nearest neighbor" estimate of pinwheel spacing.

Synthetic Pinwheel Map Generation

Several of the simulations presented in the accompanying report make use of "synthetic" orientation tuning map data generated using the method of spatially band-pass filtering two-dimensional patterns of random orientation values, as described by Rojer and Schwartz [30]. This method, mathematically equivalent to earlier "competitive-cooperative" neural network models, is a widely accepted model for cortical pinwheel patterns [54] that generates the characteristic radial arrangement of iso-orientation contours around pinwheel centers. This model is supported by Obermayer and Blasdel [55], who demonstrated that the Fourier transform of optically recorded orientation pinwheels was band-pass in characteristic, confirming the suggestion made by Rojer and Schwartz. The precise quantitative details of the pinwheel pattern are not important for the purposes of the simulations used in this experiment; rather, the generic behavior of orientation singularities, as affected by spatial filtering, is the issue.

Fig. 9 contains example MATLAB code that generates synthetic orientation tuning data, represented by the orientation field $\phi(x, y)$, using the spatial band-pass filtering method.

```
% image size (assumed square)
N = 256;

% generate uniform random angle noise
v = rand(N,N).*(2*pi);

% bandpass filter parameters
fwidth = 0.025;
fpass1 = 0.070;
fpass2 = fpass1 + fwidth;
forder = 200;

% use the MATLAB FIR machinery to make a nice bandpass filter
H = fftshift(freqz2(ftrans2(fir1(forder, [fpass1 fpass2])), [N N]));

% bandpass filtering using FFT method for convolution
x = real(ifft2( fft2(cos(v)).*H ));
y = real(ifft2( fft2(sin(v)).*H ));

% compute angle map from real and imaginary parts
phi = atan2(y, x);

% perform phase unwrapping such that 0 <= phi < 2pi
neg = find(phi < 0);
phi(neg) = phi(neg) + 2*pi;

% divide by 2 to relabel "angles" as "orientations", i.e., 0 <= phi < pi
phi = phi / 2;

% open new figure and display
figure; imagesc(phi); axis image;
```

Figure 9: Pinwheel synthesis computer script. Example MATLAB script, `pinwheel_synthesis.m`, for generating synthetic orientation tuning map data, based on the spatial band-pass filtering of random orientation values method introduced by Rojer and Schwartz [30]. Note that this implementation accounts for the phase wrapping by treating the vector-valued orientation map as a complex-valued scalar field, and filtering the real and imaginary parts independently.

Commutativity of Vector Summation and Blurring

The measurement of orientation preference maps using the optical recording technique consists of presenting the experimental subject with several orientation stimuli and imaging the exposed cortex, whose local reflectance properties are coupled to neural activity. In these experiments, the combined effects of photon scattering and optical blur result in spatial smoothing of the images acquired by the optical recording system, and these smoothed images are combined vectorially to construct the complex-valued orientation map, whose angular part is the pinwheel pattern as described above.

However, in our simulations discussed in the accompanying report of the effects of blur on the pinwheel pattern, we apply the low-pass filter directly to the complex orientation map, not the cortical reflectance images that are combined to form the complex orientation map. Since the operations of filtering and map synthesis are *commuting* linear operators, the results are the same in either order of application. That is, the order in which these operations are carried out is immaterial: "blurring then combining" or "combining then blurring" result in mathematically identical complex orientation maps. This allows us to simulate the effects of blurring the optical signals produced by the *in vivo* orientation map by directly applying blur to the complex orientation maps such as those synthesized by our spatial band-pass filtering method.

To demonstrate this equivalence, we used real optical recording data and performed the blurring and map construction in both ways. (This data was generously provided by G. Blasdel; see ref. 31.) The results are identical, as shown in Fig. 10a and 10b. Fig. 10a contains the original data set along with the corresponding pinwheel map, and Fig. 10b contains the results of blurring the optical recording data with a Cauchy kernel whose FWHM was set to 240 μm. After the data has been blurred, the pinwheel map is constructed. The result is that the resulting pinwheel map is identical whether blurring occurs before or after the map construction, and therefore the resulting map in either case exhibits the same amount of orientation singularity annihilation and movement regardless of the order of operations, as shown in Fig. 11. This demonstrates that the linear operations of "vector summation" and "spatial filtering" commute, as expected.

Acknowledgments

We thank Gary Blasdel (Northwestern University, Evanston, IL) for making us aware of the spatial blurring properties associated with the narrow depth of field achieved by the macroscope, and for generously providing us with sample optical recording data. We also thank Rick Born, Jonathan Horton, David Hubel, Niall McLoughlin, Chris Pack, and Aaron Seitz for helpful discussions related to this work. This work was supported by National Institutes of Health/National Institute of Biomedical Imaging and Bioengineering Grant EB001550. All wave optics calculations were performed using Breault Research Organization's Advanced Systems Analysis Program language. This software and training in its use was generously provided by Breault Research (Tucson, AZ). Alan Greynolds developed this software, which includes macros for the Gaussian Beam Decomposition methods used to model the macroscope optics.

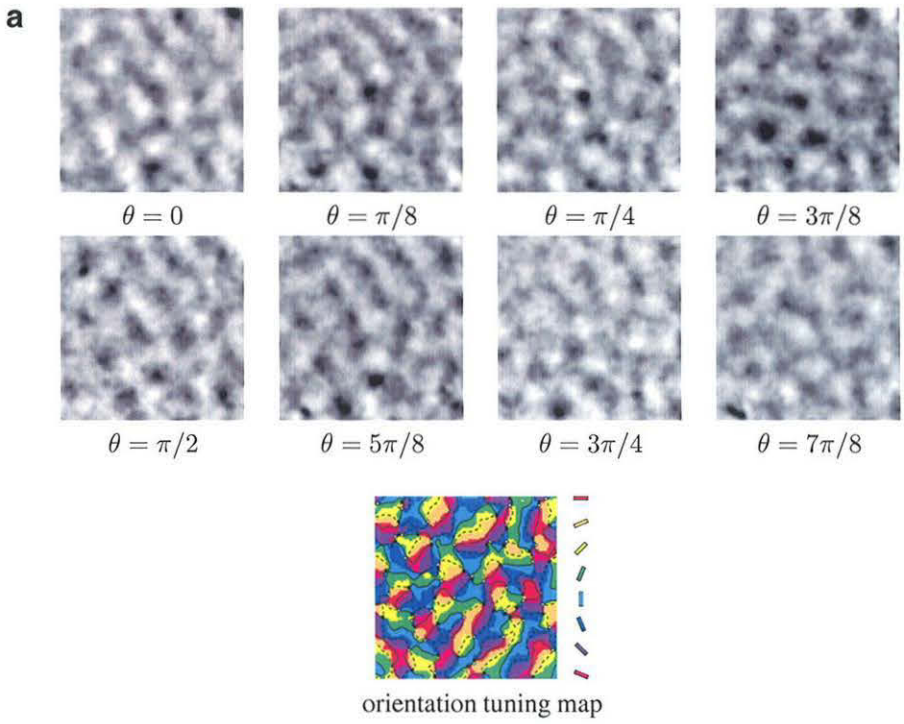

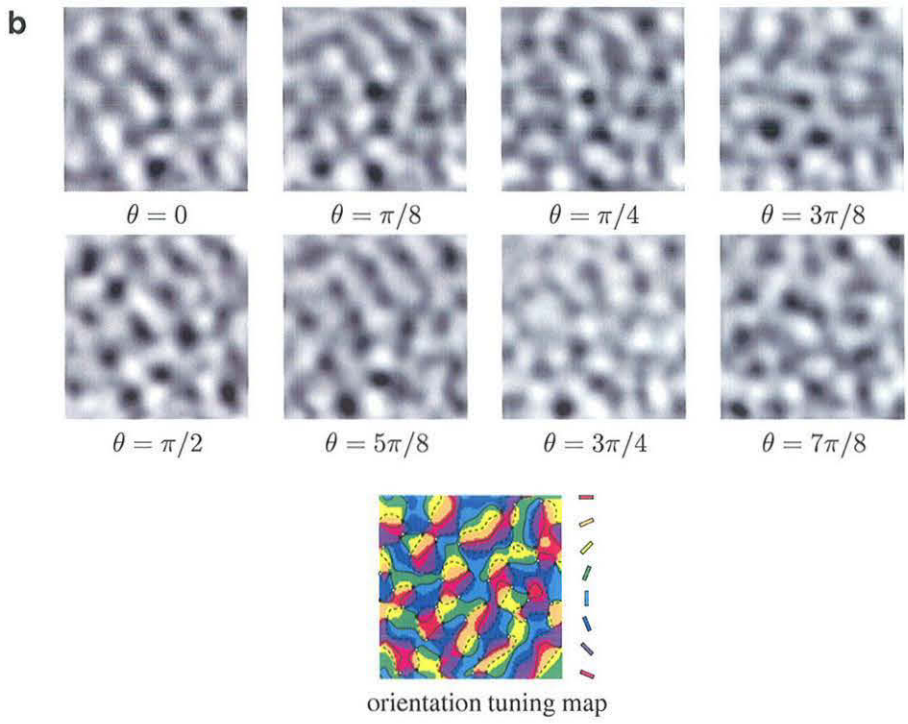

Figure 10: Commutativity of vector summation and blurring. (a) Optical recording orientation tuning data, sampled at eight orientations (above), along with the derived orientation tuning map (below). Each image represents a 4×4 mm patch of cortex. In the orientation tuning map, positive chirality (i.e., right-handed) pinwheels are indicated by *white circles* and negative chirality by *black squares*. The *solid and dashed black lines* trace out zero-crossing contours of the real and imaginary components of the complex orientation map. The pseudo-color map of orientation is depicted to the right of the orientation tuning map. (b) The result of blurring the optical recording data of (a) with a Cauchy kernel with FWHM of 240 μm. Note that the intensity in the optical recording images has been re-normalized or "stretched" to maintain high contrast. The effect of blurring the optical recording data directly is identical to that of blurring the orientation tuning map itself: orientation singularities approach one another in opposite-chirality pairs and annihilate, resulting in lower singularity density and larger distances between singularities on account of the blurring.

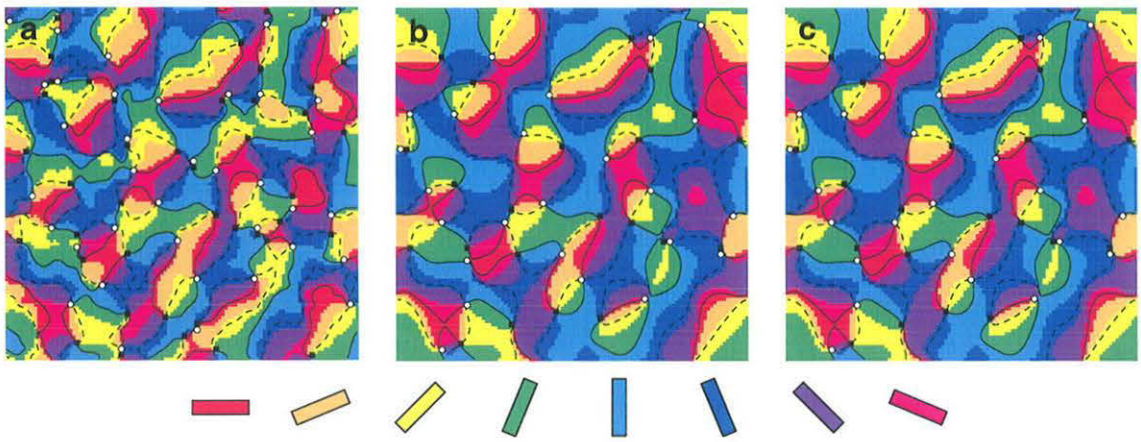

Figure 11: Comparison of "combining then blurring" with "blurring then combining". (a) Orientation tuning map computed from the original data set, as shown in Fig. 10a. The average pinwheel spacing is 540 μm (80 pinwheels). (b) Orientation tuning map resulting from blurring the complex orientation map by a Cauchy kernel of 240 μm FWHM, i.e., from "combining then blurring". The average pinwheel spacing is 667 μm, and the total number of pinwheels is 46. (c) Orientation tuning map constructed from blurred data set as shown in Fig. 10b, i.e., "blurring then combining". The average pinwheel spacing here is also 667 μm, and the total number of pinwheels is again 46. The orientation tuning maps arrived at with either method are identical.

References

1. Mountcastle, V. B. Modality and topographic organization of single neurons of cat's somatic sensory cortex. *Journal of Neurophysiology* **20**(4), 408–434 (1957).

2. Hubel, D. H. and Wiesel, T. N. Receptive fields, binocular interaction and functional architecture in the cat's visual cortex. *Journal of Physiology* **160**, 106–154 (1962).

3. Hubel, D. H. and Wiesel, T. N. Uniformity of monkey striate cortex: a parallel relationship between field size, scatter, and magnification factor. *Journal of Comparative Neurology* **158**(3), 295–305 (1974).

4. Hubel, D. H. and Wiesel, T. N. Ferrier Lecture: Functional architecture of macaque monkey visual cortex. *Proceedings of the Royal Society of London. Series B, Biological Sciences* **198**(1130), 1–59 (1977).

5. Horton, J. C. and Hubel, D. C. Regular patchy distribution of cytochrome oxidase staining in primary visual cortex of macaque monkey. *Nature* **292**(5825), 762–764 (1981).

6. Horton, J. C. Cytochrome oxidase patches: a new cytoarchitectonic feature of monkey visual cortex. *Philosophical Transactions of the Royal Society of London. Series B, Biological Sciences* **304**(1119), 255–272 (1984).

7. Horton, J. C. and Hocking, D. R. Intrinsic variability of ocular dominance column periodicity in normal macaque monkeys. *Journal of Neuroscience* **16**(22), 7228–7239 (1996).

8. Livingstone, M. S. and Hubel, D. H. Anatomy and physiology of a color system in the primate visual cortex. *Journal of Neuroscience* **4**(1), 309–356 (1984).

9. Braitenberg, V. and Braitenberg, C. Geometry of orientation columns in the visual cortex. *Biological Cybernetics* **33**(3), 179–186 (1979).

10. Blasdel, G. and Salama, G. Voltage sensitive dyes reveal a modular organisation in monkey striate cortex. *Nature* **321**(6070), 579–585 (1986).

11. Grinvald, A., Lieke, E., Frostig, R. D., Gilbert, C. D., and Wiesel, T. N. Functional architecture of cortex revealed by optical imaging of intrinsic signals. *Nature* **324**(6095), 361–364 (1986).

12. Blasdel, G. G. Orientation selectivity, preference, and continuity in monkey striate cortex. *Journal of Neuroscience* **12**(8), 3139–3161 (1992).

13. Blasdel, G. G. Topography of visual function as shown with voltage-sensitive dyes. In Sensory Processing in the Mammalian Brain: Neural Substrates and Experimental Strategies, Lund, J. S., editor, chapter 12, 242–268. Oxford University Press, New York (1989).

14. Bartfeld, E. and Grinvald, A. Relationships bwtween orientation-preference pinwheels, cytochrome oxidase blobs, and ocular dominance columns. *Proceedings of the National Academy of Sciences of the United States of America* **89**(24), 11905–11909 (1992).

15. Maldonado, P. E., Godecke, I., Gray, C. M., and Bonhoeffer, T. Orientation selectivity in pinwheel centers in cat striate cortex. *Science* **276**(6), 1551–1555 (1997).

16. Xu, X., Bosking, W., Sary, G., Stefansic, J., Shima, D., and Casagrande, V. Functional organization of visual cortex in the owl monkey. *Journal of Neuroscience* **24**(28), 6237–6247 (2004).

17. Grinvald, A. et al. In vivo optical imaging of cortical architecture and dynamics. In Modern Techniques in Neuroscience Research, Windhorst, U. and Johansson, H., editors, Springer Lab Manual, 893–969. Springer-Verlag, New York (1999).

18. Kandel, E. R., Schwartz, J. H., and Jessell, T. M., editors. *Principles of Neural Science*, 539–540. McGraw-Hill, fourth edition (2000).

19. Schwartz, E. L. and Rojer, A. S. Cortical hypercolumns and the topology of random orientation maps. In Proceedings of the 12th IAPR International Conference on Pattern Recognition, Peleg, S. and Ullman, S., editors, volume 2, 150–155 (IEEE Comput. Soc. Press, Los Alamitos, CA, 1994).

20. Schwartz, E. L. Computational studies of the spatial architecture of primate visual cortex: Columns, maps, and protomaps. In Primary Visual Cortex in Primates, Peters, A. and Rockland, K., editors, volume 10 of *Cerebral Cortex*. Plenum Press, New York (1994).

21. Orbach, H. S. and Cohen, L. B. Optical monitoring of activity from many areas of the *in vitro* and *in vivo* salamander olfactory bulb: a new method for studying functional organization in the vertebrate central nervous system. *Journal of Neuroscience* **3**(11), 2251–2262 (1983).

22. Bonhoeffer, T. and Grinvald, A. The layout of iso-orientation domains in area 18 of cat visual cortex: optical imaging reveals a pinwheel-like organization. *Journal of Neuroscience* **13**(10), 4157–4180 (1993).

23. Baker, S. and Kanade, T. Limits on super-resolution and how to break them. *IEEE Transactions on Pattern Analysis and Machine Intelligence* **24**(9), 1167–1183 (2002).

24. Elad, M. and Feuer, A. Restoration of a single superresolution image from several blurred, noisy, and undersampled measured images. *IEEE Transactions on Image Processing* **6**(12), 1646–1658 (1997).

25. Cheong, W.-F., Prahl, S. A., and Welch, A. J. A review of the optical properties of biological tissues. *IEEE Journal of Quantum Electronics* **26**(12), 2166–2185 (1990).

26. Ratzlaff, E. H. and Grinvald, A. A tandem-lens epilfuorescence macroscope: hundred-fold brightness advantage for wide-field imaging. *Journal of Neuroscience Methods* **36**(2–3), 127–137 (1991).

27. Denk, W. and Svoboda, K. Photon upmanship: why multiphoton imaging is more than a gimmick. *Neuron* **18**(3), 351–357 (1997).

28. Granquist-Fraser, D. Ph.D. dissertation (Boston Univ., Boston, MA), (2003).

29. Schiessl, I. and McLoughlin, N. Optical imaging of the retinotopic organization of V1 in the common marmoset. *NeuroImage* **20**(3), 1857–1864 (2003).

30. Rojer, A. and Schwartz, E. Cat and monkey cortical columnar patterns modeled by bandpass-filtered 2D white noise. *Biological Cybernetics* **62**(5), 381–391 (1990).

31. Tal, D. and Schwartz, E. L. Topological singularities in cortical orientation maps: the sign theorem correctly predicts orientation column patterns in primate striate cortex. *Network: Computation in Neural Systems* **8**(2), 229–238 (1997).

32. Blasdel, G. and Campbell, D. Functional retinotopy of monkey visual cortex. *Journal of Neuroscience* **21**(20), 8286–8301 (2001).

33. Ts'o, D. Y., Frostig, R. D., Lieke, E. E., and Grinvald, A. Functional organization of primate visual cortex revealed by high resolution optical imaging. *Science* **249**(4967), 417–420 (1990).

34. Vnek, N., Ramsden, B. M., Hung, C. P., Goldman-Rakic, P. S., and Roe, A. W. Optical imaging of functional domains in the cortex of the awake and behaving monkey. *Proceedings of the National Academy of Sciences of the United States of America* **96**(7), 4057–4060 (1999).

35. Grinvald, A. and Hildesheim, R. VSDI: a new era in functional imaging of cortical dynamics. *Nature Reviews Neuroscience* **5**(11), 874–885 (2004).

36. Deng, X. and Gu, M. Penetration depth of single-, two-, and three-photon fluorescence microscopic imaging through human cortex structures: Monte Carlo simulation. *Applied Optics* **42**(16), 3321–3329 (2003).

37. Preparata, F. P. and Shamos, M. I. *Computational Geometry: An Introduction.* Springer-Verlag, New York, (1985).

38. Prahl, S. A., Keijzer, M., Jacques, S. L., and Welch, A. J. A Monte Carlo model of light propagation in tissue. In Dosimetry of Laser Radiation in Medicine and Biology, Mueller, G. and Sliney, D., editors, volume IS 5, 102–111. SPIE Optical Engineering Press, Bellingham, WA (1989).

39. Metropolis, N. and Ulam, S. The Monte Carlo method. *Journal of the American Statistical Association* **44**(247), 335–341 (1949).

40. Tuchin, V. V. *Tissue optics: light scattering methods and instruments for medical diagnosis.* SPIE Optical Engineering Press, Bellingham, WA, (2000).

41. Splinter, R., Cheong, W. F., van Gemert, M. J., and Welch, A. J. In vitro optical properties of human and canine brain and urinary bladder tissues at 633 nm. *Lasers in Surgery and Medicine* **9**(1), 37–41 (1989).

42. Yaroslavsky, A. N., Schulze, P. C., Yaroslavsky, I. V., Schober, R., Ulrich, F., and Schwarzmaier, H. J. Optical properties of selected native and coagulated human brain tissues *in vitro* in the visible and near infrared spectral range. *Physics in Medicine and Biology* **47**(12), 2059–2073 (2002).

43. Womelsdorf, T., Eysel, U. T., and Kisvarday, Z. F. Comparison of orientation maps obtained with different number of stimulus orientations. *NeuroImage* **13**(6 Pt 1), 1131–1139 (2001).

44. Henyey, L. G. and Greenstein, J. L. Diffuse radiation in the galaxy. *Astrophysical Journal* **93**, 70–83 (1941).

45. Witt, A. N. Multiple scattering in reflection nebulae I. A Monte Carlo approach. *Astrophysical Journal* **S35**, 1–6 (1977).

46. Smith, W. J. *Modern Lens Design: A Resource Manual.* McGraw Hill, New York, (1992).

47. Fujioka, Y. Camera lens system with long back focal distance and large aperture ratio. U.S. Patent 4,443,070, (1981).

48. Flock, S. T., Jacques, S. L., Wilson, B. C., Star, W. M., and van Gemert, M. J. Optical properties of Intralipid: a phantom medium for light propagation studies. *Lasers in Surgery and Medicine* **12**(5), 510–519 (1992).

49. Arnaud, J. A. Non-orthogonal optical waveguides and resonators. *Bell System Technical Journal* **49**, 2311 (1970).

50. Eadie, W. T., Drijard, D., James, F. E., Roos, M., and Sadoulet, B. *Statistical Methods in Experimental Physics.* North Holland, (1971).

51. Freund, I. and Shvartsman, N. Wave-field phase singularities: the sign principle. *Physical Review A (Atomic, Molecular, and Optical Physics)* **50**(6), 5164–5172 (1994).

52. Berry, M. V. and Dennis, M. R. Phase singularities in isotropic random waves. *Proceedings of the Royal Society of London, Series A (Mathematical, Physical and Engineering Sciences)* **456**(2001), 2059–2079 (2000).

53. Erwin, E., Obermeyer, K., and Schulten, K. A comparison of models of visual cortical map formation. In Computation and Neural Systems, Eeckman, F. and Bower, J., editors, 137–150. Kluwer Academic Publishers, Boston, MA (1993).

54. Swindale, N. V. The development of topography in the visual cortex: a review of models. *Network* **7**(2), 161–247 (1996).

55. Obermayer, K. and Blasdel, G. G. Geometry of orientation and ocular dominance columns in monkey striate cortex. *Journal of Neuroscience* **13**(10), 4114–1429 (1993).